PHYSICAL REVIEW C **108**, 014619 (2023)

One-neutron transfer from ^{16}O to ^{27}Al and ^{28}Si targets at $E_{\mathrm{lab}} = 240$ MeV

R. Linares,[1] C. C. Seabra,[1] V. A. B. Zagatto,[1] F. Cappuzzello,[2,3] M. Cavallaro,[2] D. Carbone,[2]
C. Agodi,[2] L. M. Fonseca,[4] and J. R. B. Oliveira[5]

[1] *Instituto de Física, Universidade Federal Fluminense, Niterói - Rio de Janeiro, 24210-346, Brazil*
[2] *Istituto Nazionale di Fisica Nucleare, Laboratori Nazionali del Sud, CT-95123 Catania, Italy*
[3] *Dipartimento di Fisica e Astronomia "Ettore Majorana", Università di Catania, CT-95123, Italy*
[4] *Technische Universität Darmstadt, Fachbereich Physik, Institut für Kernphysik, 64289 Darmstadt, Germany*
[5] *Instituto de Física, Universidade de São Paulo, São Paulo 05508-090, Brazil*

(Received 15 May 2023; accepted 11 July 2023; published 28 July 2023)

Background: Transfer reactions induced by heavy ions have been explored to study the role of pairing in the two-nucleon transfers. However, many reaction channels are often open and couplings between them must be considered. Some of these couplings are effectively taken by suitable optical potentials whereas other channels are explicitly considered into the coupling scheme. The interplay between optical potentials and coupling schemes may lead to ambiguities in the interpretation of transfer mechanisms.

Purpose: Relevant parameters in the calculations can be constrained by several reactions measured under the same experimental conditions. This may lead to a unified theoretical reaction scheme that can be applied to properly judge the role of sequential and simultaneous processes in the two-nucleon transfers.

Methods: In this work we analyze the one-neutron transfer reactions to ^{27}Al and ^{28}Si induced by (^{16}O, ^{15}O) at $E_{\mathrm{lab}} = 240$ MeV. The choice of targets is of particular interest: within the weak coupling model, the ^{27}Al can be interpreted as a proton hole coupled to the ^{28}Si core. The parameters of the optical potentials to describe the elastic and inelastic scattering in these reactions have been studied in a previous publication. Here, we focus on the reaction and nuclear structure models to describe the experimental cross sections. We performed coupled channel Born approximation (CCBA) and coupled reaction channels (CRC) using spectroscopic amplitudes obtained from shell model with three different interactions and single-particle model spaces.

Results: The optical potentials and coupling schemes provide a good description of the angular distributions of the cross sections, in which the CRC calculations give a slightly better agreement with experimental than the CCBA one. We compare CRC calculations using spectroscopic amplitudes from three different shell-model interactions. They all give a reasonable description of the experimental data except for the transfer that populates the $7/2^-_1$ state in ^{29}Si. This requires a $1f_{7/2}$ single-particle state, present only in the model space for one of the considered interactions.

Conclusions: Within the same theoretical methodology, we are able to achieve an overall good description of the experimental data for one-neutron transfer in the ^{27}Al(^{16}O, ^{15}O)^{28}Al and ^{28}Si(^{16}O, ^{15}O)^{29}Si at 240 MeV. This methodology will be adopted to study the proton transfer channels in these systems in a future work.

DOI: 10.1103/PhysRevC.108.014619

I. INTRODUCTION

One-nucleon transfer reaction is an important source of information about the single particle nature of nuclear states. This information is usually quantified by spectroscopic factors (SFs) or asymptotic normalization coefficients (ANCs), which are the norm of the overlap function between a nucleus (A) in a state i with a nucleus $A + 1$ in a state f. Measurements of the one-nucleon transfer cross sections are related to these SFs and ANCs, although the connection between them is not straightforward [1,2]. Additionally, the angular distribution of these cross sections can be used to study the quantum numbers of the valence particle.

In the past, a vast majority of studies was carried out using the (d, p), (p, d), (^{3}He, d), and (d, ^{3}He) probes. Reasons for choosing light projectiles are twofold. From the experimental standpoint, measurements of light ejectiles typically attain high energy resolution, good particle identification, and a clear distinction between low-lying states of the residual nuclei. From the theoretical standpoint, reaction dynamic is usually treated within the distorted-wave Born approximation (DWBA), which basically assumes that elastic scattering is the most relevant reaction channel and couplings to individual nonelastic channels are weak and not strongly correlated with each other. However, some works have addressed the importance of a three-body approach to interpret the (d, p) data [3,4], and the nonlocality of the nucleon-nucleus interactions [5]. The latter can be replaced by a suitable local equivalent potential. When reaction and structure models are in place, a good agreement between experimental and theoretical cross sections is usually achieved. The ratio of experimental to theoretical cross sections is usually adopted as experimental estimation for the SFs. It has been shown these estimates, extracted within the adiabatic distorted-wave approximation (ADWA) for the (d, p) reaction in many target nuclei, give a remarkable good agreement with SFs obtained from large-scale shell models [6]. Transfer with the (d, p) reaction is indeed a useful tool for spectroscopic studies of unstable nuclei and Ref. [7] gives a clear overview.

Nowadays, modern experimental setups, often featuring large acceptance spectrometers and multiparameter detectors, provide high-quality particle identification and energy resolution for heavy ejectiles. These have increased the use of heavy-ion transfer reactions (HI-TR) as a tool for gaining deeper insights into nuclear reactions and structure. A topic of interest is the role of pairing in the two-nucleon transfer reactions. These reactions can proceed through a sequential, in which states in an intermediary mass partition are populated, and a simultaneous mechanisms. Moreover, it can selectively populate some nuclear states in the target-like nucleus and, therefore, pinpoint nuclear states strongly characterized by a two-particle system in the nuclear mean field. The selectivity in the population of nuclear states in ^{14}C has been shown in [8]. The excitation energy spectra of ^{14}C populated by the ^{12}C(^{18}O, ^{16}O) reaction favors the population of well-known two neutrons in the *sd* shell coupled to a ^{12}C, such as the 2_+ at 7.01 and 8.32 MeV and the 4_+ at 10.74 MeV. These states are barely populated with the ^{13}C(^{18}O, ^{17}O) reaction.

Theoretical models to interpret HI-TR are a challenge by themselves. Heavy-ion reactions are absorptive and couplings to nonelastic reaction channels are usually strong. This means that the DWBA approach is no longer valid and requires consistent reaction models that properly capture the effects of most relevant channels and their couplings. In recent publications [9–15], we have pursued the goal of exploring HI-TR through a systematic analysis. In these works, the cross sections for elastic and inelastic scatterings are used to constrain the parameters of the optical potentials and the strengths of the couplings to inelastic channels. These parameters are then used in the transfer reaction calculations. The nuclear structure ingredient is taken from shell model, quasirandom phase approximation, or interacting boson model calculations. It is explicitly assumed that the information about the nuclear structure is independent of the reaction probe. So, in principle, SFs deduced from electron induced $(e, e'p)$ knockout, nucleon-nucleus reactions, and HI-TR are comparable. However, it is worth highlighting that SFs extracted from knock-out reactions are about 30% less than most large-scale shell model values. This experimental-to-theory deviation is referred as quenching of the SFs and may have its origin in the long- and short-range correlations of nucleons in the nuclear medium [16]. Recently, it has been shown, for the proton- and neutron-removal reactions from the ^{14}O nucleus at 100 MeV/u, that inelastic and transfer reactions may contribute as much as 50% to the experimental cross sections, resulting in a steeper dependence of the SFs on the Fermi-surface asymmetry [17].

Interpretations of nuclear reaction mechanisms must consider the limitations of the optical potentials and the coupling schemes. Given the lack of a global model, one must evaluate the suitability of interaction parameters for the specific system under investigation. To refine the theoretical predictions, it is essential to compare them with experimental data, which can offer valuable constraints to improve the reliability of such calculations. This expedient has been adopted to interpret experimental cross sections measured for single charge exchange reactions in the ^{40}Ca(^{18}O, ^{18}F) ^{40}K [13] and ^{116}Cd(^{20}Ne, ^{20}F) ^{116}In [14].

In this paper we present new experimental data for the one-neutron transfer to ^{28}Si and ^{27}Al induced by the (^{16}O, ^{15}O) probe at $E_{\mathrm{lab}} = 240$ MeV. These target nuclei were chosen because: (i) within the weak coupling, the ^{27}Al can be interpreted as a proton hole coupled to the ^{28}Si core, therefore they can be treated within the same nuclear structure model; (ii) both target nuclei have the same number of neutrons and the $1d_{5/2}$ neutron sub-shell filled in their ground states. The elastic and inelastic scatterings for these systems have been analyzed previously in Ref. [18] and the coupled channel calculations satisfactorily reproduce the experimental data. The elastic and inelastic scatterings of the $^{16}\mathrm{O} + {}^{27}\mathrm{Al}$ system have been also studied at $E_{\mathrm{lab}} = 100$ MeV [19] and at $E_{\mathrm{lab}} = 280$ MeV [20], with very good agreement between data and calculations. Here, the same optical potential and couplings to inelastic channels in the entrance mass partition are considered and we focus on the results of coupled-channel Born approximation (CCBA) and coupled reaction channels (CRC) to the one-neutron transfer to the target nuclei.

This paper is organized as follows. In Sec. II we give a brief overview on the experimental details and in Sec. III we present the theoretical analysis. Section IV presents our discussions based on comparisons between data and calculations. Conclusions are given in Sec. V.

II. EXPERIMENTAL DETAILS

The experimental details are given in Ref. [18] and here we just summarize some information. The measurements were performed at the *Istituto Nazionale di Fisica Nucleare - Laboratori Nazionali del Sud*, Catania, Italy. The 240 MeV $^{16}\mathrm{O}^{6+}$ beam was delivered by the superconducting cyclotron. A ^{27}Al (89 $\mu\mathrm{g/cm}^2$ thickness) and a ^{28}Si (148 $\mu\mathrm{g/cm}^2$ thickness) self-supporting foils were used. The $^{15}\mathrm{O}^{8+}$ projectile-like particles from the one-neutron transfer reaction were momentum analyzed by the MAGNEX spectrometer [21–24] set in the full acceptance mode ($\Omega \sim 50$ msr). Parameters of the final trajectory of the $^{15}\mathrm{O}^{8+}$ particles were measured by the focal plane detector. Measurements were carried out with the spectrometer optical axis set at two angles, $\theta_{\mathrm{lab}} = 3^\circ$ and 8°. Due to the large angular acceptance of the spectrometer, these measurements cover angles in the $0^\circ < \theta_{\mathrm{lab}} < 12^\circ$ range. Trajectory reconstruction of $^{15}\mathrm{O}^{8+}$ detected particles is performed by solving the equations of motion, through the magnetic fields of the dipole and the quadrupole, and calculates the kinematics parameters relative to the target position, such as the excitation energy and the scattering angle θ_{lab}. Further details of this procedure are given in Refs. [21,22,25,26]. The overall angular resolution achieved in these measurements is 0.6° (in the center of mass) and the energy resolution,

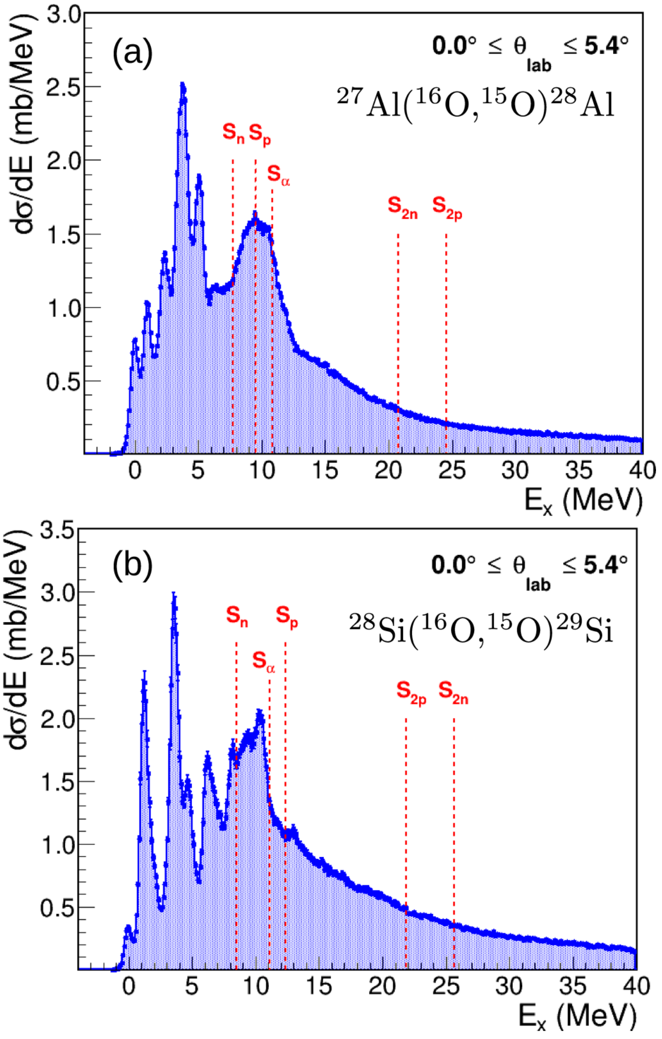

FIG. 1. Energy differential cross-section spectra obtained for (^{16}O, ^{15}O) one-neutron stripping reaction at 240 MeV in ^{27}Al target, that populates states in ^{28}Al nucleus (a) and in ^{28}Si target, that populates states in ^{29}Si nucleus (b).

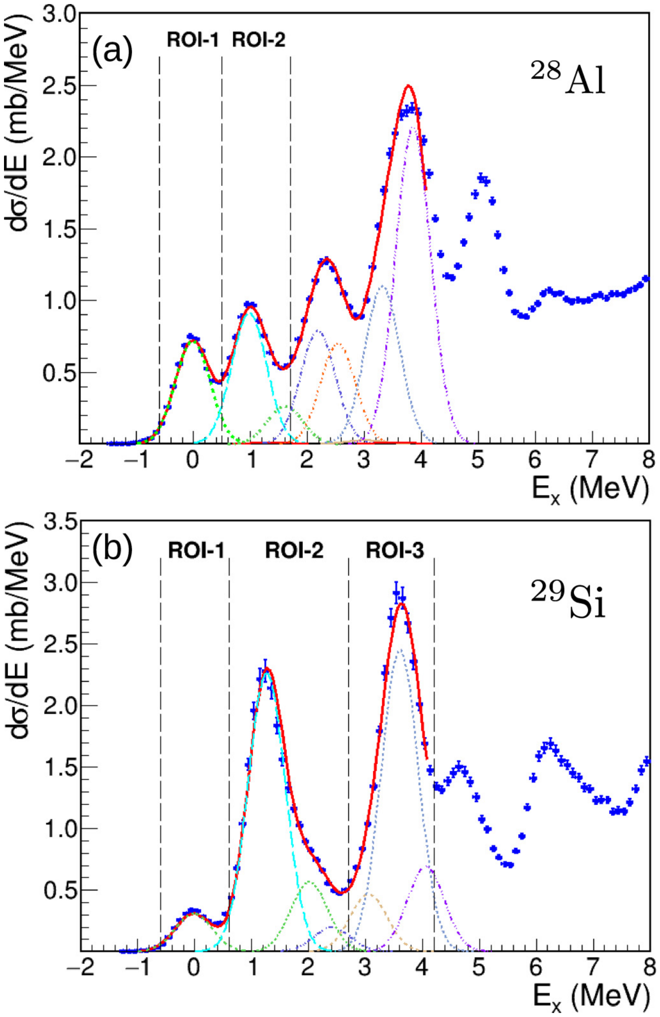

FIG. 2. Detailed view of the excitation energy spectra at low-lying states for ^{28}Al (a) and ^{29}Si (b). Continuous red curves correspond to a multi-gaussian fittings to the experimental data points whereas the colored gaussian curves under the fit represent the individual contributions. The experimental cross sections are determined for the region of interest (ROI) indicated in each spectrum.

defined as the full width at half-maximum (FWHM), is about 0.6 MeV.

The excitation energy spectra in the residual nuclei, namely ^{28}Al and ^{29}Si, are shown in Fig. 1. The vertical axis corresponds to the energy differential cross section with 0.1 MeV energy step and both spectra are integrated from $0^\circ < \theta_{\text{lab}} < 5.4^\circ$. According to Brink's rule [27], matching conditions for high energy transfer reactions favor excitation of states around 1–3 MeV in both cases. These low-lying states are relatively well populated up to ~6 MeV, followed by an almost continuous population of states beyond the neutron separation energy (S_n). Separation energies are also indicated in the spectra. A closer view of the low-lying states in the ^{28}Al and the ^{29}Si excitation energy spectra is shown in Fig. 2. The solid red lines correspond to a multi-gaussian fitting to the experimental data points. The individual states, that compose the multi-gaussian curve, are represented by colored gaussian curves in Fig. 2. Centroids of individual gaussian curves were set according to known excitation energies [28,29]. Standard deviation, which is associated to the experimental energy resolution (FWHM = 0.6 MeV), were set equal for all individual gaussian curves. The number of states in the ^{28}Al nucleus is large and, beyond 2.0 MeV, we selected some states to compose the multi-gaussian fit. For the ^{29}Si nucleus, all known states up to 3.9 MeV are included. The good quality achieved by the multi-gaussian fitting shows that the experimental spectra are consistent with known states for the target-like nuclei ^{28}Al and ^{29}Si. In the ^{29}Si excitation energy spectrum Fig. 2(b), the $3/2_1^+$ and $7/2_1^-$ states, respectively, at 1.27 MeV and 3.62 MeV, are well populated. This has been also observed in the ^{28}Si(^{18}O, ^{17}O) ^{29}Si reaction at $E_{\text{lab}} = 84$ MeV (see Ref. [30]).

The experimental energy resolution does not allow to distinguish between two successive individual states in most cases. Therefore, we are reporting the cross sections for the

TABLE I. Details of the regions of interest adopted in the excitation energy spectra for the target-like ^{28}Al and ^{29}Si nuclei.

Residual nucleus	ROI	Energy range (MeV)	States J^π (MeV)
^{28}Al	1	[−0.6; +0.5]	3_1^+ (g.s.), 2_1^+ (0.03)
	2	[+0.6; +1.7]	0_1^+ (0.97), 3_2^+ (1.01), 1_1^+ (1.37), 1_2^+ (1.620), 2_2^+ (1.623)
^{29}Si	1	[−0.6; +0.5]	$1/2_1^+$ (g.s.)
	2	[+0.6; +2.6]	$3/2_1^+$ (1.27), $5/2_1^+$ (2.03), $3/2_2^+$ (2.43)
	3	[+2.7; +4.2]	$5/2_2^+$ (3.07), $7/2_1^-$ (3.62), $7/2_1^+$ (4.08)

regions of interest (ROIs), as indicated by vertical dashed black lines in Fig. 2. The energy range and states considered in each ROI are indicated in Table I. Carbon and oxygen are possible contaminant elements on these targets. Reactions with the possible ^{12}C contaminant produce a ground-to-ground transition peak at $E_x \sim 3.6$ MeV, in the ^{28}Al energy excitation spectrum, and at $E_x \sim 4.2$ MeV, in the ^{29}Si energy excitation spectrum. Reactions with the possible ^{16}O contaminant would produce ground-to-ground transition peaks at even higher excitation energies. No clear evidence of these contaminant contributions are seen in the excitation energy spectra. Nevertheless, we avoid extracting experimental cross sections for these energies.

The one-neutron stripping angular differential cross sections were determined from integration in the energy range of each ROI. The error bars in the cross sections correspond to uncertainty in the solid angle determination and counting statistics. A systematic uncertainty in the cross section of 10%, coming from uncertainties in the target thickness and beam integration by the Faraday cup, is common to all the angular distribution points and is not included in the error bars. Angular distributions of the experimental cross sections are shown in Sec. IV.

III. THEORETICAL ANALYSIS

Calculations within the CCBA and the CRC frameworks were performed using the FRESCO code [31] with exact finite range and prior representation. Nonorthogonality corrections and full complex remnant terms were considered in the coupled channel equations. The coupling scheme considered for each system is represented in Fig. 3.

For the optical potential, we adopted $U(r) = [1.0 + iN_i] \times V_{\rm SPP}(r)$, where $V_{\rm SPP}(r)$ is the double-folding São Paulo potential (SPP) [32–34]. The SPP uses matter densities described as two-parameter Fermi distributions with matter radius, defined as $R_m = 1.31A^{1/3} - 0.84$ fm, and matter diffuseness, set to $a_m = 0.56$ fm. These were determined from a systematic study for many nuclei [34]. In [18], within coupled-channel formalism, we have shown that best agreement between calculations and the experimental data for the elastic and inelastic scatterings in the ^{27}Al + ^{16}O and the ^{28}Si + ^{16}O systems requires increasing the matter diffuseness, in the two-parameter Fermi distribution, to $a_m = 0.62$ fm for both ^{27}Al and ^{28}Si nuclei. Also, the strength of the imaginary part was set to $N_i = 0.6$, for the ^{27}Al + ^{16}O, and $N_i = 0.7$, for the ^{28}Si + ^{16}O systems. For consistency, we have maintained this choice also here. In the exiting mass partitions, since we do not have experimental data for elastic scattering for the ^{28}Al + ^{15}O and the ^{29}Si + ^{15}O systems, we adopted the standard SPP, with $a_m = 0.56$ fm. But even so, we performed some calculations using the modified version of the SPP (i.e., $a_m = 0.62$ fm) as the optical potential in the exiting mass partitions. Theoretical transfer cross sections with the modified SPP are reduced by 32%, compared to the standard, and the shapes of the angular distributions are very similar. The same reduction is attained using the standard SPP but increasing N_i, since the strength of

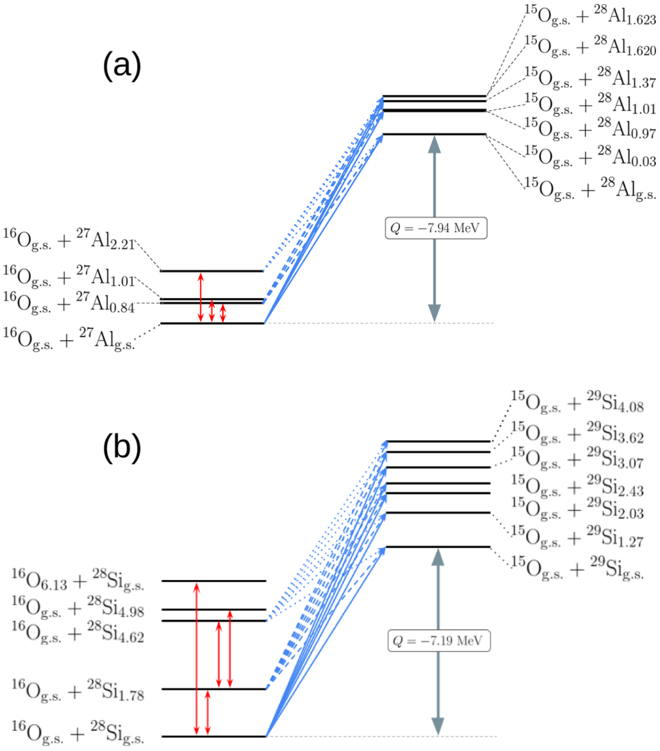

FIG. 3. Coupling schemes adopted in the calculations of the one-neutron transfer in the ^{27}Al(^{16}O, ^{15}O)^{28}Al (a) and ^{28}Si(^{16}O, ^{15}O)^{29}Si (b) reactions. Red arrows indicate the couplings considered in the initial mass partition, while the blue arrows indicate the couplings introduced within the CCBA reaction scheme. In the CRC framework, all arrows have to be considered bidirectional (see text).

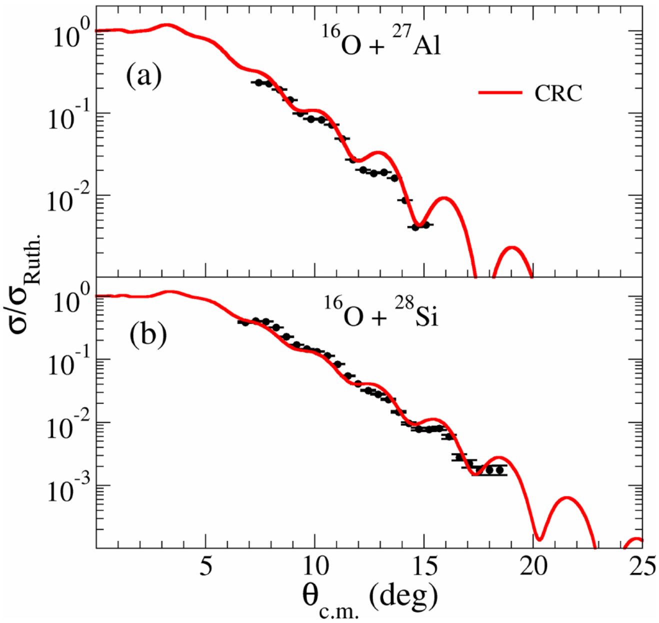

FIG. 4. Comparison between CRC and experimental data for the elastic scatterings in the ^{27}Al + ^{16}O (a) and ^{28}Si + ^{16}O (b) systems. Experimental data from Ref. [18].

the potential around the radius of the system (about 7.2 fm) is relevant. The strength of the imaginary part will be mentioned in the next subsections.

Couplings to inelastic channels are included through the deformation of the optical potential (both real and imaginary parts) in which the intrinsic matrix elements for these transitions were calculated from the experimental reduced transition probabilities $B(E2)$.

The single-particle wave functions were calculated assuming the valence neutron bound to a core, represented by an effective binding potential with the Woods-Saxon shape. The depth of this binding potential is changed to reproduce the binding energies for each state. The reduced radius and diffuseness of the binding potential are set to 1.20 fm and 0.60 fm, respectively, to describe the valence neutron bound to the ^{15}O core. These values have been adopted in previous works on transfer reactions induced by heavy ions [12,15,30,35]. For the ^{28}Al and the ^{29}Si target-like nuclei, we adopt 1.26 fm and 0.70 fm for the reduced radius and diffuseness, respectively. These values are suitable to describe the transfer cross section in ^{19}F and ^{29,30}Si [12,36]. We have performed some tests with different values for the reduced radius and the diffuseness parameters, within 5% deviation. The absolute values of the theoretical transfer cross sections systematically changes within 20% but the overall shapes of the angular distributions are not appreciably affected by the parameters of the binding potentials.

The SFs were obtained using the NuShellX code [37]. For ^{15,16}O, the calculations were performed using the PSDMOD interaction [38], that is a modified version in the *p-sd* part of the WBT interaction (so-called *psdwbt* interaction)

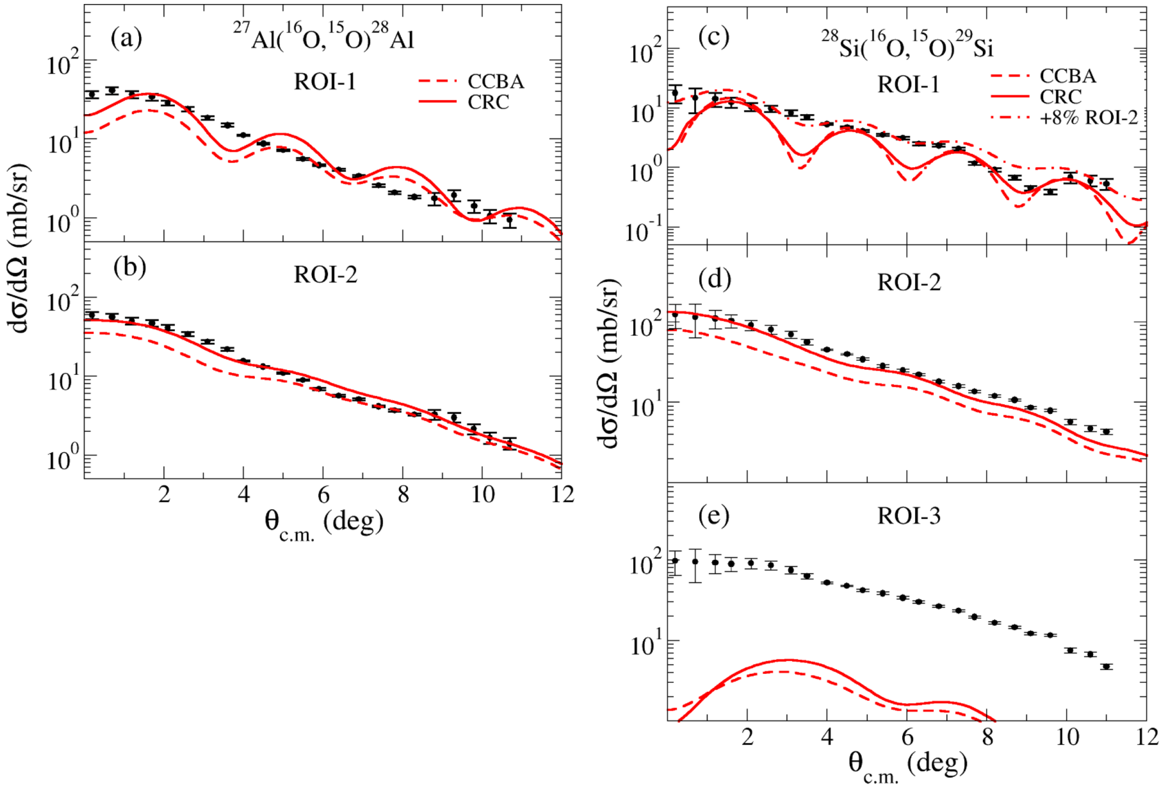

FIG. 5. Comparisons between experimental and theoretical cross sections for one-neutron transfer in the ^{27}Al(^{16}O, ^{15}O) ^{28}Al reaction (a) and (b) and the ^{28}Si(^{16}O, ^{15}O) ^{29}Si reaction [(c)–(e)]. Theoretical curves obtained within the CCBA and CRC approaches using spectroscopic amplitudes obtained from the PSDMOD interaction.

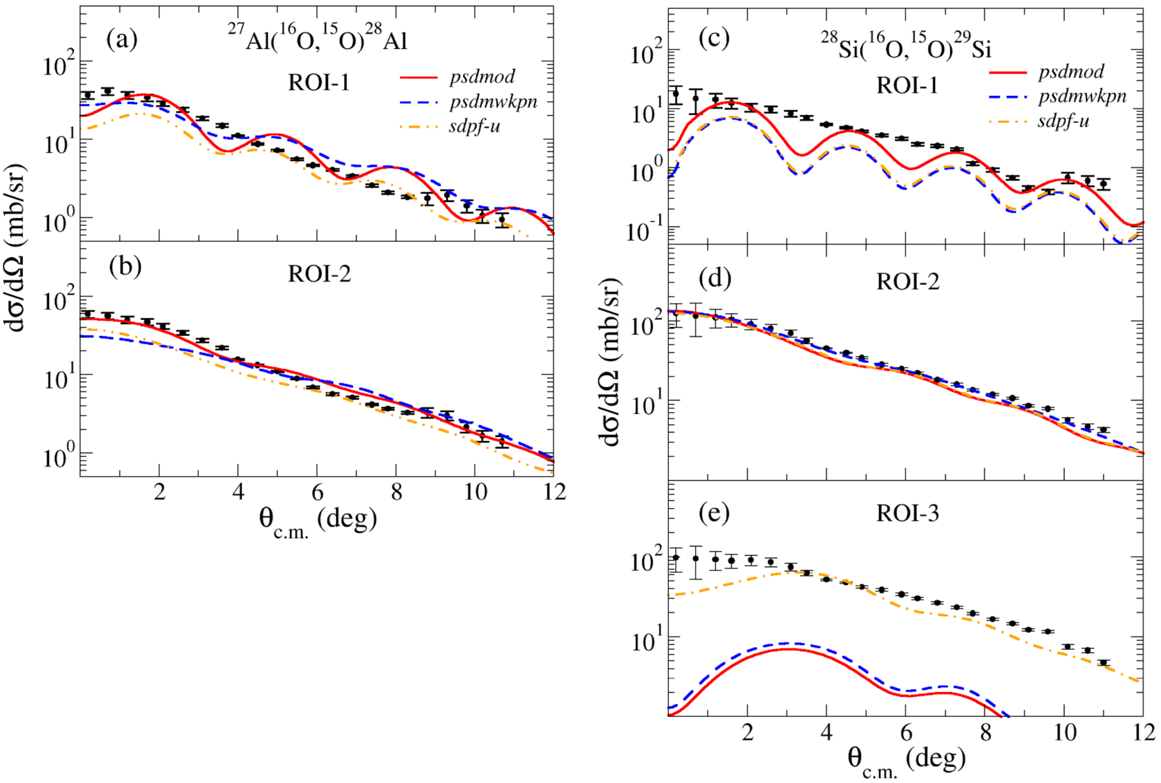

FIG. 6. Angular distribution of the experimental cross sections for one-neutron stripping in the ^{27}Al(^{16}O, ^{15}O) ^{28}Al system for the ROI-1 (a), ROI-2 (b), and ROI-3 (c) considered. The curves are CRC calculations using SFs from the PSDMOD (solid red), PSDMWKPN (dashed blue), and SDPF-U (dot-dashed orange) interactions.

[39]. This gives a reasonable description of some properties (energy levels, spin-parity, dipole magnetic moments, probabilities for γ transitions, and β decay) for the p-sd-shell nuclei. For ^{27,28}Al and ^{28,29}Si isotopes, three interactions are considered:

(1) the PSDMOD interaction (previously described), with a model space that assumes ^{4}He as a closed core and valence neutrons and protons in the $1p_{3/2}$, $1p_{1/2}$, $1d_{5/2}$, $1d_{3/2}$, and $2s_{1/2}$ shells;
(2) the PSDMWKPN interaction, that is a combination of the Cohen-Kurath interaction [40] for the p shell, the Wildenthal interaction [41] for the sd shell and the Millener-Kurath interaction [42] for the coupling matrix elements between p and sd shells. The model space assumes a ^{4}He core with valence neutrons and protons in the $1p_{3/2}$, $1p_{1/2}$, $1d_{5/2}$, $1d_{3/2}$, and $2s_{1/2}$ shells;
(3) the SDPF-U interaction, which is a modified version of the SDPF-NR interaction [43] with improvements in the description of the monopole part [44]. This interaction describes nucleons at the $1d_{5/2}$, $1d_{3/2}$, $2s_{1/2}$, $1f_{7/2}$, $1f_{5/2}$, $2p_{3/2}$, and $2p_{1/2}$ subshells, assuming a ^{16}O core.

The spectroscopic amplitudes for the Al and Si isotopes are shown in Tables II and III, respectively (see Appendix). Spectroscopic amplitudes obtained within the PSDMOD interaction and the adopted model space successfully describe the two-neutron transfer in the ^{28}Si(^{18}O, ^{16}O) ^{30}Si reaction [36]. The one-neutron transfer in the ^{28}Si(^{18}O, ^{17}O) ^{29}Si [30] and in the ^{28}Si(^{13}C, ^{12}C) ^{29}Si reactions, are slightly better reproduced using spectroscopic amplitudes from the PSDMWKPN interaction. Besides these two interactions, we also included the SDPF-U interaction because of the $1f_{7/2}$ shell, that is necessary to describe the $7/2^{-}_{1}$ (3.62 MeV) state in the ^{29}Si. As one may observe, the SDPF-U interaction considers an ^{16}O core, while the PSDMOD and PSDMWKPN consider a ^{4}He one. We also performed some checks assuming a ^{16}O core with the PSDMOD and the PSDMWKPN interactions. Spectroscopic amplitudes obtained with the heavier core are very similar, with average deviation less than 5%, compared to the values reported in the tables.

IV. DISCUSSIONS

A. The CCBA and CRC calculations

As a starting point, we check the consistency of our couplings and optical potentials in the CCBA and CRC calculations by looking back the elastic cross sections, previously published in [18]. For the elastic channel, the CCBA and CRC calculations show no difference within the explored angular range and, therefore, in Fig. 4 we present the CRC curves only, which is also very similar to the coupled channel calculations presented in [18]. In the elastic channel we see no difference between CRC calculations using spectroscopic amplitudes obtained with the PSDMOD, PSDMWKPN, and SDPF-U interactions. Our calculations reproduce well

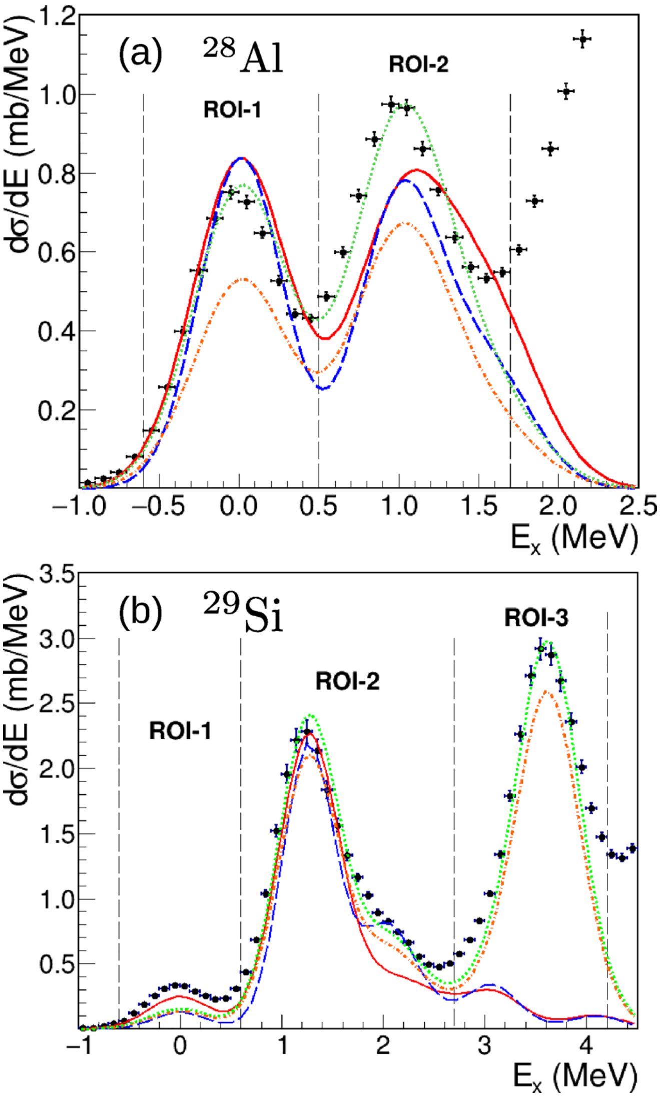

FIG. 7. Comparisons between theoretical and experimental differential cross sections for the low-lying states for ^{28}Al (a) and ^{29}Si (b). Continuous red, dashed blue, and dot-dashed orange curves correspond the theoretical spectra generated from the cross sections given by the CRC calculations with PSDMOD, PSDMWKPN, and SDPF-U interactions, respectively. Dotted green curves correspond to a scaled SPDF-U spectra. Further details in the text.

oscillation observed in the experimental data and is a good indication that the optical potentials and couplings in the entrance mass partition are in place.

The transfer cross sections are shown in Fig. 5, for both the ^{27}Al(^{16}O, ^{15}O)^{28}Al Figs. 5(a) and 5(b) and the ^{28}Si(^{16}O, ^{15}O)^{29}Si reactions Figs. 5(c) to 5(e). The experimental angular resolution (FWHM = 0.6°) is considered by a convolution of the DWBA/CRC curves and a gaussian function. Here, we consider spectroscopic amplitudes obtained with the PSDMOD interaction only. Comparatively, couplings between channels in the entrance and exiting mass partitions, considered within the CRC approach, result in a small increase of the cross sections compared with the CCBA values. Nevertheless, the overall shape of the angular distribution of the cross section are similar. The ground-to-ground transitions for the $^{27}\mathrm{Al} + {}^{16}\mathrm{O}$ Fig. 5(a) and the $^{28}\mathrm{Si} + {}^{16}\mathrm{O}$ systems Fig. 5(c) exhibit oscillations that are not observed in the experimental data. It seems that couplings between channels in the exit mass partition, that are not included in our coupling scheme, may attenuate this oscillation. However this requires further investigation of the deformation parameters that describe these couplings and the optical potential. In the case of the $^{28}\mathrm{Si} + {}^{16}\mathrm{O}$ system, there is a contribution from the tail of the state at 1.27 MeV, in the ROI-2. The effect of this contribution is represented by the dot-dashed curve in Fig. 5(c), for which this tail contributes about 8% of the cross section for the ROI-1. We also point out that the theoretical cross sections for ROI-3 Fig. 5(e) are well below the experimental data because the adopted model space in the shell model do not include the $1f_{7/2}$ subshell, necessary to describe the $7/2^-$ state in ^{29}Si. The strength of the imaginary part of the optical potentials in the exiting mass partitions affect the theoretical curves in such way that the overall shapes are preserved. Reducing the imaginary part, which corresponds to reducing the flux taken away, systematically increases the calculated transfer cross sections. The overall best agreement between experimental data and theoretical curve is achieved for the CRC calculations and $N_i = 0.6$ for the optical potential in the exiting mass partitions. We then proceed with the CRC calculations in the next subsection.

B. Spectroscopic amplitudes from different interactions

In this subsection we focus on the spectroscopic amplitudes obtained with the three different interactions, namely PSDMOD, PSDMWKPN, and SDPF-U, within the CRC approach. A comparison between calculations and experimental data is shown in Fig. 6 for both the ^{27}Al(^{16}O, ^{15}O)^{28}Al Figs. 5(a) and 5(b) and the ^{28}Si(^{16}O, ^{15}O)^{29}Si reactions Figs. 5(c) to 5(e). The results with the PSDMOD, PSDMWKPN, and SDPF-U spectroscopic amplitudes are practically the same in all channels, except for ROI-3 in the ^{28}Si(^{16}O, ^{15}O)^{29}Si reaction. It is clear that the $1f_{7/2}$ single-particle shell is important to describe the shape of the experimental angular distribution of the cross sections.

Besides an angular distribution of the cross section, we can explore the energy differential spectra, shown in Fig. 2, as a second element to judge the quality of the calculations. This is an approach that can be used together with the angular distribution of the transfer cross sections as indication for the consistency of theoretical framework. The CRC cross sections integrated within $0° < \theta_{\mathrm{lab}} < 5.4°$ (which correspond to $0° < \theta_{\mathrm{c.m.}} < 8.4°$) for each transfer channel are used as input to define the parameters of a gaussian curve that represents this channel in an energy spectra. The centroid and standard deviation of the gaussian curve are given by the known excitation energy and the experimental energy resolution (FWHM = 0.6 MeV), respectively. The amplitude is calculated so that the energy integration of this theoretical gaussian curve reproduces the corresponding CRC cross section. All states indicated in Table I are included and the *theoretical* energy differential cross spectra is generated by summing all these gaussian curves.

TABLE II. Spectroscopic amplitudes adopted for the Al isotopes.

^{27}Al nucleus		^{28}Al nucleus			Spec. Ampl. $\mathcal{S}$		
state (MeV)	J^π	state (MeV)	J^π	$n\ell_j$	PSDMOD	PSDMWKPN	SDPF-U
g.s.	$5/2^+$	g.s.	3^+	$2s_{1/2}$	0.714	−0.662	−0.673
		g.s.	3^+	$1d_{3/2}$	0.303	−0.058	−0.059
		g.s.	3^+	$1d_{5/2}$	0.209	−0.292	−0.290
		0.03	2^+	$2s_{1/2}$	−0.594	0.467	−0.496
		0.03	2^+	$1d_{3/2}$	0.523	−0.522	0.495
		0.03	2^+	$1d_{5/2}$	−0.168	0.203	−0.203
		0.97	0^+	$1d_{5/2}$	0.358	0.451	0.458
		1.01	3^+	$2s_{1/2}$	−0.301	−0.077	0.076
		1.01	3^+	$1d_{3/2}$	0.757	0.722	−0.760
		1.01	3^+	$1d_{5/2}$	−0.184	−0.171	0.149
		1.37	1^+	$1d_{3/2}$	0.558	−0.460	0.424
		1.37	1^+	$1d_{5/2}$	−0.092	−0.034	0.074
		1.620	1^+	$1d_{3/2}$	−0.042	0.041	0.083
		1.620	1^+	$1d_{5/2}$	−0.189	0.193	0.036
		1.623	2^+	$2s_{1/2}$	−0.396	−0.160	0.145
		1.623	2^+	$1d_{3/2}$	−0.605	−0.318	0.310
		1.623	2^+	$1d_{5/2}$	−0.097	−0.332	0.340
0.84	$1/2^+$	g.s.	3^+	$1d_{5/2}$	0.236	0.324	0.323
		0.03	2^+	$1d_{3/2}$	0.131	0.131	−0.126
		0.03	2^+	$1d_{5/2}$	0.025	0.022	−0.024
		0.97	0^+	$2s_{1/2}$	0.668	−0.586	−0.608
		1.01	3^+	$1d_{5/2}$	−0.271	0.232	−0.209
		1.37	1^+	$2s_{1/2}$	0.401	0.406	−0.437
		1.37	1^+	$1d_{3/2}$	−0.237	−0.230	0.170
		1.620	1^+	$2s_{1/2}$	−0.174	−0.068	0.008
		1.620	1^+	$1d_{3/2}$	−0.480	−0.541	−0.532
		1.623	2^+	$2s_{1/2}$	0.213	−0.041	0.052
		1.623	2^+	$1d_{3/2}$	−0.047	0.153	−0.164
1.01	$3/2^+$	g.s.	3^+	$1d_{3/2}$	0.001	0.017	0.020
		g.s.	3^+	$1d_{5/2}$	0.329	0.386	0.386
		0.03	2^+	$2s_{1/2}$	0.010	0.024	−0.029
		0.03	2^+	$1d_{3/2}$	0.136	0.172	−0.180
		0.03	2^+	$1d_{5/2}$	−0.135	−0.178	0.203
		0.97	0^+	$1d_{3/2}$	−0.232	0.267	0.255
		1.01	3^+	$1d_{3/2}$	0.019	−0.010	0.030
		1.01	3^+	$1d_{5/2}$	−0.269	0.131	−0.151
		1.37	1^+	$2s_{1/2}$	0.088	−0.003	0.002
		1.37	1^+	$1d_{3/2}$	0.103	0.155	−0.202
		1.37	1^+	$1d_{5/2}$	0.035	0.146	−0.171
		1.620	1^+	$2s_{1/2}$	−0.075	−0.101	−0.234
		1.620	1^+	$1d_{3/2}$	−0.493	−0.465	0.459
		1.620	1^+	$1d_{5/2}$	−0.091	−0.052	0.053
		1.623	2^+	$2s_{1/2}$	0.216	−0.427	0.460
		1.623	2^+	$1d_{3/2}$	0.106	0.101	−0.123
		1.623	2^+	$1d_{5/2}$	−0.073	0.299	−0.297
2.21	$7/2^+$	g.s.	3^+	$2s_{1/2}$	−0.017	−0.035	−0.036
		g.s.	3^+	$1d_{3/2}$	0.149	0.212	0.218
		g.s.	3^+	$1d_{5/2}$	0.406	0.358	0.368
		0.03	2^+	$1d_{3/2}$	0.151	0.200	−0.204
		0.03	2^+	$1d_{5/2}$	−0.454	−0.427	0.437
		1.01	3^+	$2s_{1/2}$	0.059	−0.044	0.046
		1.01	3^+	$1d_{3/2}$	−0.116	0.108	−0.096
		1.01	3^+	$1d_{5/2}$	0.064	−0.199	0.186
		1.37	1^+	$1d_{5/2}$	0.081	0.091	−0.127
		1.620	1^+	$1d_{5/2}$	−0.442	−0.467	−0.522
		1.623	2^+	$1d_{3/2}$	0.109	−0.318	0.284
		1.623	2^+	$1d_{5/2}$	0.077	−0.250	0.281

TABLE III. Spectroscopic amplitudes adopted for the Si isotopes.

^{28}Si nucleus		^{29}Si nucleus			Spec. Ampl. $\mathcal{S}$		
state (MeV)	J^π	state (MeV)	J^π	$n\ell_j$	PSDMOD	PSDMWKPN	SDPF-U
g.s.	0^+	g.s.	$1/2^+$	$2s_{1/2}$	0.716	0.570	0.584
		1.27	$3/2^+$	$1d_{3/2}$	−0.827	−0.806	0.791
		2.03	$5/2^+$	$1d_{5/2}$	−0.347	−0.451	0.442
		2.43	$3/2^+$	$1d_{3/2}$	0.046	0.007	−0.029
		3.07	$5/2^+$	$1d_{5/2}$	−0.226	−0.247	−0.246
		3.62	$7/2^-$	$1f_{7/2}$	–	–	−0.628
1.78	2^+	g.s.	$1/2^+$	$1d_{3/2}$	−0.388	−0.479	−0.468
		g.s.	$1/2^+$	$1d_{3/2}$	−0.847	−0.857	−0.864
		1.27	$3/2^+$	$2s_{1/2}$	−0.090	−0.019	0.068
		1.27	$3/2^+$	$1d_{3/2}$	−0.006	0.027	−0.010
		1.27	$3/2^+$	$1d_{5/2}$	0.293	0.345	−0.323
		2.03	$5/2^+$	$2s_{1/2}$	0.632	0.562	−0.580
		2.03	$5/2^+$	$1d_{3/2}$	0.025	−0.037	0.026
		2.03	$5/2^+$	$1d_{5/2}$	0.414	−0.478	−0.474
		2.43	$3/2^+$	$2s_{1/2}$	−0.341	−0.247	0.281
		2.43	$3/2^+$	$1d_{3/2}$	0.748	0.764	−0.752
		2.43	$3/2^+$	$1d_{5/2}$	−0.518	−0.587	0.580
		3.07	$5/2^+$	$2s_{1/2}$	0.013	−0.003	0.011
		3.07	$5/2^+$	$1d_{3/2}$	−0.761	−0.742	−0.758
		3.07	$5/2^+$	$1d_{5/2}$	0.052	−0.034	0.049
		3.62	$7/2^-$	$1f_{7/2}$	–	–	0.706
		4.08	$7/2^+$	$1d_{3/2}$	0.732	0.749	0.750
		4.08	$7/2^+$	$1d_{5/2}$	0.173	0.232	0.224
4.62	4^+	1.27	$3/2^+$	$1d_{5/2}$	0.904	0.645	−0.748
		2.03	$5/2^+$	$1d_{3/2}$	−0.425	0.452	0.481
		2.03	$5/2^+$	$1d_{5/2}$	−0.195	0.201	0.356
		2.43	$3/2^+$	$1d_{5/2}$	0.295	0.309	−0.390
		3.07	$5/2^+$	$1d_{3/2}$	−0.244	−0.074	−0.105
		3.07	$5/2^+$	$1d_{5/2}$	0.406	0.666	0.647
		3.62	$7/2^-$	$1f_{7/2}$	–	–	−0.237
		4.08	$7/2^+$	$2s_{1/2}$	−0.369	0.298	−0.296
		4.08	$7/2^+$	$1d_{3/2}$	0.072	−0.093	0.120
		4.08	$7/2^+$	$1d_{5/2}$	−0.243	0.338	−0.335

The comparison between theoretical and experimental energy differential cross-section spectra is shown in Fig. 7. Here, we emphasize that small deviations between calculations and experimental data are not clear in log-scale, adopted in Figs. 5 and 6, but evident in linear scales, as shown in Fig. 7. However, the most important point addressed with this comparison is the profiles of theoretical and experimental spectra.

In Fig. 7(a), we show that the PSDMOD and PSDMWKPN spectroscopic amplitudes produce structures with similar amplitudes in the ROI-1 and -2, whereas the experimental spectrum shows that the amplitude of the peak in ROI-2 is higher than the one in ROI-1. This is best reproduced by the SDPF-U spectra (dot-dashed orange curve), although the absolute values of the energy differential cross sections are low. The dotted green curve represents the SPDF-U spectra scaled by a factor 1.45. The agreement between this curve and the experimental data points is quite clear. The SDPF-U spectra also gives a very good description of the experimental data points in the ^{28}Si(^{16}O, ^{15}O) ^{29}Si reaction see Fig. 7(b). In this spectrum, the dotted green curve represent the SDPF-U spectra scaled by a factor 1.15. We highlight the region around $E_x = 2.0$ MeV, where the SPDMOD and SPDMWKPN spectra not describe the shape of the experimental data. All theoretical curves underestimate the energy differential cross section in the ROI-1.

Although the CRC calculations with the SDPF-U spectroscopic amplitudes underestimate the experimental cross sections, it gives a good overall description of the shape in the angular distribution and the energy differential cross sections. A systematic increase of the transfer cross sections can be induced in the CRC calculation by: (i) decreasing the imaginary part of the optical potential in the exiting mass partition and (ii) increasing the reduced radius or diffuseness of the binding potential. From our point of view, these expedients should be adopted within a consistent description of other reaction channels and, for this reason, we are not discussing in this work.

V. CONCLUSIONS

Understanding of the transfer mechanisms in HI-TR demands a systematic, both experimentally and theoretically, study of many reaction channels that are usually open. In this context it is important to achieve a global description of data for as many reactions as possible (elastic, inelastic, and transfer cross sections). In this work we analyze the one-neutron transfer to ^{27}Al and ^{28}Si induced by the (^{16}O, ^{15}O) probe at $E_{\text{lab}} = 240$ MeV. Comparisons between these systems take advantage of similarities in the nuclear structure of the target-like nuclei, since the ^{27}Al can be interpreted as a proton hole coupled to the ^{28}Si core. Moreover, both nuclei have the $1d_{5/2}$ neutron subshell filled in their ground states.

Parameters of the optical potentials and couplings in the entrance mass partition have been defined from the elastic and inelastic cross sections, in a previous work. The theoretical methodology adopted for the calculation of the one-neutron transfer cross sections is based on recent works with HI-TR, in which the parameters for the binding potential are set accordingly.

The agreement between theory and experimental data is good for the ^{28}Si(^{16}O, ^{15}O)$\,^{29}$Si reaction. It is observe that the $1f_{7/2}$ single-particle shell is important to describe the $7/2^-$ state in ^{29}Si and the angular distribution of the cross sections for the ROI-3. On the other hand, the oscillatory behavior predicted by the calculations is not observed mostly due to finite angular resolution in the experimental data.

We explore the energy differential spectra to judge the overall quality of our CRC calculation. This is an approach that combined with the angular distribution of the cross sections refines interpretations of the calculations. For the reactions studied in this work, the CRC calculations using SDPF-U spectroscopic amplitudes gives the best overall agreement even though the absolute values of the cross sections are below the experimental ones.

ACKNOWLEDGMENTS

The Brazilian authors acknowledge the following foundations for financial support: CNPq (Grants No. 317451/2021-9, No. 304750/2021-2, and No. 316019/2021-6), INCT-FNA (Instituto Nacional de Ciência e Tecnologia - Física Nuclear e Aplicações) Proc. No. 464898/2014-5. J.R.B.O. also acknowledges funding from FAPESP, Grant No. 2019/07767-1. L.M.F. also acknowledge support by TU Darmstadt-GSI cooperation contract.

APPENDIX: SPECTROSCOPIC AMPLITUDES

Spectroscopic amplitudes for Al and Si can be found in Tables II and III, respectively.

---

[1] A. M. Mukhamedzhanov and F. M. Nunes, Phys. Rev. C **72**, 017602 (2005).

[2] D. Y. Pang, F. M. Nunes, and A. M. Mukhamedzhanov, Phys. Rev. C **75**, 024601 (2007).

[3] F. M. Nunes, A. Deltuva, and J. Hong, Phys. Rev. C **83**, 034610 (2011).

[4] M. Gomez-Ramos and A. M. Moro, Phys. Rev. C **95**, 044612 (2017).

[5] N. K. Timofeyuk and R. C. Johnson, Phys. Rev. Lett. **110**, 112501 (2013).

[6] M. B. Tsang, J. Lee, and W. G. Lynch, Phys. Rev. Lett. **95**, 222501 (2005).

[7] N. Timofeyuk and R. Johnson, Prog. Part. Nucl. Phys. **111**, 103738 (2020).

[8] M. Cavallaro, F. Cappuzzello, M. Bondì, D. Carbone, V. N. Garcia, A. Gargano, S. M. Lenzi, J. Lubian, C. Agodi, F. Azaiez, M. De Napoli, A. Foti, S. Franchoo, R. Linares, D. Nicolosi, M. Niikura, J. A. Scarpaci, and S. Tropea, Phys. Rev. C **88**, 054601 (2013).

[9] A. Spatafora, F. Cappuzzello, D. Carbone, M. Cavallaro, J. A. Lay, L. Acosta, C. Agodi, D. Bonanno, D. Bongiovanni, I. Boztosun, G. A. Brischetto, S. Burrello, S. Calabrese, D. Calvo, E. R. Chávez Lomelí, I. Ciraldo, M. Colonna, F. Delaunay, N. Deshmukh, J. L. Ferreira, V. A. B. Zagatto *et al.* (for the NUMEN Collaboration), Phys. Rev. C **100**, 034620 (2019).

[10] D. Carbone, R. Linares, P. Amador-Valenzuela, S. Calabrese, F. Cappuzzello, M. Cavallaro, S. Firat, M. Fisichella, A. Spatafora, L. Acosta, C. Agodi, I. Boztosun, G. A. Brischetto, D. Calvo, E. R. Chávez-Lomelí, I. Ciraldo, M. Cutuli, F. Delaunay, N. Deshmukh, P. Finocchiaro *et al.*, Universe **7**, 58 (2021).

[11] L. La Fauci, A. Spatafora, F. Cappuzzello, C. Agodi, D. Carbone, M. Cavallaro, J. Lubian, L. Acosta, P. Amador-Valenzuela, T. Borello-Lewin, G. A. Brischetto, S. Calabrese, D. Calvo, V. Capirossi, E. R. Chávez-Lomelí, I. Ciraldo, M. Cutuli, F. Delaunay, H. Djapo, C. Eke *et al.* (NUMEN Collaboration), Phys. Rev. C **104**, 054610 (2021).

[12] O. Sgouros, M. Cavallaro, F. Cappuzzello, D. Carbone, C. Agodi, A. Gargano, G. De Gregorio, C. Altana, G. A. Brischetto, S. Burrello, S. Calabrese, D. Calvo, V. Capirossi, E. R. Chávez-Lomelí, I. Ciraldo, M. Cutuli, F. Delaunay, H. Djapo, C. Eke, P. Finocchiaro, V. A. B. Zagatto *et al.* (for the NUMEN Collaboration), Phys. Rev. C **104**, 034617 (2021).

[13] M. Cavallaro, J. I. Bellone, S. Calabrese, C. Agodi, S. Burrello, F. Cappuzzello, D. Carbone, M. Colonna, N. Deshmukh, H. Lenske, A. Spatafora, L. Acosta, P. Amador-Valenzuela, T. Borello-Lewin, G. A. Brischetto, D. Calvo, V. Capirossi, E. Chávez, I. Ciraldo, M. Cutuli *et al.*, Front. Astron. Space Sci. **8**, 659815(2021).

[14] S. Burrello, S. Calabrese, F. Cappuzzello, D. Carbone, M. Cavallaro, M. Colonna, J. A. Lay, H. Lenske, C. Agodi, J. L. Ferreira, S. Firat, A. Hacisalihoglu, L. La Fauci, A. Spatafora, L. Acosta, J. I. Bellone, T. Borello-Lewin, I. Boztosun, G. A. Brischetto, D. Calvo, V. A. B. Zagatto *et al.* (NUMEN Collaboration), Phys. Rev. C **105**, 024616 (2022).

[15] I. Ciraldo, F. Cappuzzello, M. Cavallaro, D. Carbone, S. Burrello, A. Spatafora, A. Gargano, G. DeGregorio, R. I. Magaña Vsevolodovna, L. Acosta, C. Agodi, P. Amador-Valenzuela, T. Borello-Lewin, G. A. Brischetto, S. Calabrese, D. Calvo, V. Capirossi, E. R. Lomeli, M. Colonna, F. Delaunay, H. Djapo, C. Eke, P. Finocchiaro, S. Firat, M. Fisichella, A. Foti, A. Hacisalihoglu, F. Iazzi, L. LaFauci, R. Linares, N. H. Medina, M. Moralles, J. R. B. Oliveira, A. Pakou, L. Pandola, H. Petrascu, F. Pinna, G. Russo, E. Santopinto, O. Sgouros, M. A. Guazzelli, S. O. Solakci, V. Soukeras, G. Souliotis, D. Torresi, S. Tudisco, A. Yildirim, and V. A. B. Zagatto (for the NUMEN Collaboration), Phys. Rev. C **105**, 044607 (2022).

[16] T. Aumann, C. Barbieri, D. Bazin, C. Bertulani, A. Bonaccorso, W. H. Dickhoff, A. Gade, M. Gómez-Ramos, B. Kay, A. Moro, T. Nakamura, A. Obertelli, K. Ogata, S. Paschalis, and T. Uesaka, Prog. Part. Nucl. Phys. **118**, 103847 (2021).

[17] T. Pohl, Y. L. Sun, A. Obertelli, J. Lee, M. Gómez-Ramos, K. Ogata, K. Yoshida, B. S. Cai, C. X. Yuan, B. A. Brown, H. Baba, D. Beaumel, A. Corsi, J. Gao, J. Gibelin, A. Gillibert, K. I. Hahn, T. Isobe, D. Kim, Y. Kondo *et al.*, Phys. Rev. Lett. **130**, 172501 (2023).

[18] L. M. Fonseca, R. Linares, V. A. B. Zagatto, F. Cappuzzello, D. Carbone, M. Cavallaro, C. Agodi, J. Lubian, and J. R. B. Oliveira, Phys. Rev. C **100**, 014604 (2019).

[19] D. Pereira, J. Lubian, J. Oliveira, D. Sousa, and L. Chamon, Phys. Lett. B **670**, 330 (2009).

[20] F. Cappuzzello, D. Nicolosi, R. Linares, J. R. B. Oliveira, J. Lubian, C. Agodi, D. Carbone, M. Cavallaro, P. N. de Faria, A. Foti, and M. R. D. Rodrigues, Eur. Phys. J. A **52**, 169 (2016).

[21] A. Lazzaro, F. Cappuzzello, A. Cunsolo, M. Cavallaro, A. Foti, A. Khouaja, S. Orrigo, and J. Winfield, Nucl. Instrum. Methods Phys. Res. A **570**, 192 (2007).

[22] A. Lazzaro, F. Cappuzzello, A. Cunsolo, M. Cavallaro, A. Foti, S. Orrigo, M. Rodrigues, and J. Winfield, Nucl. Instrum. Methods Phys. Res. A **591**, 394 (2008).

[23] A. Cunsolo, F. Cappuzzello, M. Cavallaro, A. Foti, A. Khouaja, S. E. A. Orrigo, J. S. Winfield, L. Gasparini, G. Longo, T. Borello-Lewin, M. R. D. Rodrigues, M. D. L. Barbosa, C. Nociforo, and H. Petrascu, Eur. Phys. J. Spec. Top. **150**, 343 (2007).

[24] F. Cappuzzello, C. Agodi, D. Carbone, and M. Cavallaro, Eur. Phys. J. A **52**, 167 (2016).

[25] F. Cappuzzello, C. Agodi, M. Bondì, D. Carbone, M. Cavallaro, A. Cunsolo, M. D. Napoli, A. Foti, D. Nicolosi, S. Tropea, P. N. de Faria, R. Linares, J. R. B. Oliveira, and M. R. D. Rodrigues, Nucl. Instrum. Methods Phys. Res. A **763**, 314 (2014).

[26] D. Carbone, Eur. Phys. J. Plus **130**, 143 (2015).

[27] D. M. Brink, *Semi-classical Methods for Nucleus-Nucleus Scattering* (Cambridge University Press, Cambridge, 1985).

[28] M. Shamsuzzoha Basunia, Nucl. Data Sheets **113**, 909 (2012).

[29] M. S. Basunia, Nucl. Data Sheets **114**, 1189 (2013).

[30] R. Linares, M. J. Ermamatov, J. Lubian, F. Cappuzzello, D. Carbone, E. N. Cardozo, M. Cavallaro, J. L. Ferreira, A. Foti, A. Gargano, B. Paes, G. Santagati, and V. A. B. Zagatto, Phys. Rev. C **98**, 054615 (2018).

[31] I. J. Thompson, Comput. Phys. Rep. **7**, 167 (1988).

[32] M. A. Cândido Ribeiro, L. C. Chamon, D. Pereira, M. S. Hussein, and D. Galetti, Phys. Rev. Lett. **78**, 3270 (1997).

[33] L. C. Chamon, D. Pereira, M. S. Hussein, M. A. Candido Ribeiro, and D. Galetti, Phys. Rev. Lett. **79**, 5218 (1997).

[34] L. C. Chamon, B. V. Carlson, L. R. Gasques, D. Pereira, C. De Conti, M. A. G. Alvarez, M. S. Hussein, M. A. Cândido Ribeiro, E. S. Rossi, Jr., and C. P. Silva, Phys. Rev. C **66**, 014610 (2002).

[35] R. Linares, C. C. Seabra, V. A. B. Zagatto, V. Scarduelli, L. Gasques, L. C. Chamon, B. R. Gonçalves, D. R. Mendes. Junior, and A. Lépine-Szily, Phys. Rev. C **101**, 014611 (2020).

[36] E. N. Cardozo, J. Lubian, R. Linares, F. Cappuzzello, D. Carbone, M. Cavallaro, J. L. Ferreira, A. Gargano, B. Paes, and G. Santagati, Phys. Rev. C **97**, 064611 (2018).

[37] W. D. M. Rae, http://www.garsington.eclipse.co.uk (2008).

[38] Y. Utsuno and S. Chiba, Phys. Rev. C **83**, 021301(R) (2011).

[39] E. K. Warburton and B. A. Brown, Phys. Rev. C **46**, 923 (1992).

[40] S. Cohen and D. Kurath, Nucl. Phys. **73**, 1 (1965).

[41] B. Wildenthal, Prog. Part. Nucl. Phys. **11**, 5 (1984).

[42] D. Millener and D. Kurath, Nucl. Phys. A **255**, 315 (1975).

[43] S. Nummela, P. Baumann, E. Caurier, P. Dessagne, A. Jokinen, A. Knipper, G. Le Scornet, C. Miehé, F. Nowacki, M. Oinonen, Z. Radivojevic, M. Ramdhane, G. Walter, J. Äystö, and ISOLDE Collaboration, Phys. Rev. C **63**, 044316 (2001).

[44] F. Nowacki and A. Poves, Phys. Rev. C **79**, 014310 (2009).